JOURNAL OF SOLID STATE CHEMISTRY 111, 370–379 (1994)

Competition of Covalency between Cr^{III}–O and Ta^{V}–O Bonds in the Perovskites Ca_2CrTaO_6 and Sr_2CrTaO_6

Jin-Ho Choy, Jae-Hyun Park, Seung-Tae Hong, and Dong-Kuk Kim

Department of Chemistry, College of Natural Sciences, Seoul National University, Seoul 151-742, Korea

Received June 18, 1993; in revised form October 4, 1993; accepted October 12, 1993

According to the Rietveld refinement, the perovskites Ca_2CrTaO_6 and Sr_2CrTaO_6 are found to have space groups $P2_1/n$ (monoclinic, a = 5.4199(1) Å, b = 5.4936(1) Å, c = 7.7108(2) Å, and β = 90.02(1)°) and $Fm\bar{3}m$ (cubic, a = 7.8837(1) Å), respectively, with partial disordering of Cr and Ta ions. Structural analysis indicated that the Cr–O bond distance is shorter than the Ta–O distance in both compounds. XANES for Ta L_{III} edge and EPR spectroscopic analyses and magnetic susceptibility measurements were performed to obtain information on the covalency between B cations (B = Cr, Ta) and oxygen ions. The variation of crystal structure and magnetic properties in the two compounds could be explained by the size and the covalent bonding nature between metal and oxygen ions.

INTRODUCTION

The crystal structure of $A_2BB'O_6$- or $AA'BB'O_6$-type perovskites depends upon the size of the A- or B-site cations, the electronic structure of the transition metal ions (usually B-site cations), and the character of the covalent bonding between metal and oxygen ions. In general, the size of the A ion influences the crystal symmetry significantly, while that of the B ion does not change the symmetry, but changes the lattice volume proportionally (1–3). The variation of crystal structure with ionic size may be understood in terms of the Goldschmidt tolerance factor

$$t = d(A\text{–O})/\sqrt{2}d(B\text{–O}),$$

where $d(A$–O) and $d(B$–O) are the bond lengths. Ideal cubic perovskite occurs for t = 1. At lower t values, distortions from cubic structure are found. The electronic configuration of the B ion may influence the structure. Typical examples are A_2CuWO_6 with A = Sr and Ba (4), which have a tetragonal structure. Such a structural distortion can be explained by the strong crystal field stabilization energy for the tetragonally distorted octahedron. The covalent bonding forces of the metal–ligand bond are also responsible for lattice deformation (5) and for the magnetic and optical properties (6) of transition metal compounds.

It was pointed out that in ABO_3 perovskite the O–2p orbitals that π-bond with the B cation also σ-bond with the A cation. In addition, the O–2p orbitals that σ-bond with the B cation also σ-bond with the B' cation in an ordered $AA'BB'O_6$-type perovskite. Thus, $\pi(B$–O) and $\sigma(A$–O) bonds compete with each other, and $\sigma(B$–O) and $\sigma(B'$–O) bonds are also in competition (7–10). Therefore, the covalency of the (B–O) bond is influenced by the nature of both the A and the B' cations, and it can be deduced that for a given B' cation the B–O covalency will be affected only by the A cation, that is, the size and chemical bonding nature of the A cation.

Therefore, we have been interested in the evolution of covalency with respect to A-cation substitution in some ordered $AA'B^{II}B'^{V}O_6$-type perovskites. According to our previous experimental results, the covalency of the B'–O bond is influenced more significantly than that of the (B–O) bond by the A-cation substitution (11, 12). Such a result comes from the stronger covalency of the B'–O bond than of the B–O bond due to the shift of oxygen ions toward the more highly charged cation, B'(V). Similarly, in the $A_2B^{III}B'^{V}O_6$-type perovskite (A = alkaline earth metal ions, B,B' = transition metal ions), the B–O bond is expected to be less influenced than the B'–O bond by the substitution of A cations since the B-cation valence is lower than the B' valence. A number of such perovskites have been reported so far (1, 13–16). Among them, we thought that it would be interesting to study the structural evolution of $A_2Cr^{III}Ta^{V}O_6$ with A-cation substitution from Ca to Sr and to Ba, since the Cr–O bond is expected to be as covalent as the Ta–O bond due to the strong crystal field stabilization energy for the Cr^{III} ion in the octahedral site. Although Ca_2CrTaO_6 (13), Sr_2CrTaO_6 (14, 15), and Ba_2CrTaO_6 (16) are known to have orthorhombic, cubic, and 8-layer hexagonal structures, respectively, no systematic physical and chemical characterizations have been performed as yet.

In this paper, the synthesis and characterization of the perovskites Ca_2CrTaO_6 and Sr_2CrTaO_6 are described us-

0022-4596/94 $6.00

ing various techniques such as powder X-ray diffraction, electron paramagnetic resonance spectroscopy, magnetic susceptibility measurement, and X-ray absorption near-edge structure (XANES) spectroscopy. Because the structure of hexagonal Ba_2CrTaO_6 is completely different from those of Ca_2CrTaO_6 and Sr_2CrTaO_6, only the latter two compounds have been considered in this study. In particular, in order to confirm and compare the bonding nature in the two compounds, the exact structural data including the bond lengths and bond angles were estimated by means of the Rietveld X-ray technique.

EXPERIMENTAL

The polycrystalline sample of Ca_2CrTaO_6 was prepared from high-purity $CaCO_3$, Cr_2O_3, and Ta_2O_5. The stoichiometric mixture was ground thoroughly in an agate mortar with small amounts of ethanol, dried, pelleted, and prefired in an alumina boat at 1100°C for 20 hr under N_2. For the preparation of the Sr derivative, $Sr(NO_3)_2$ was used instead of $CaCO_3$. The strontium nitrate was dissolved in water with chromium and tantalum oxides and heated at 700–800°C for 1 hr to convert it into an oxide. The samples were finely ground, pelleted, and prefired at 1100°C for 12 hr under N_2. This procedure (grinding, pelletizing, and firing at 1350°C) was repeated until single-phase perovskite could be obtained in the X-ray diffraction pattern. The total reaction times at 1350°C were 20 and 15 hr for Ca and Sr compounds, respectively.

Powder X-ray diffraction patterns were recorded using a MAC Science MPX 18 X-ray diffractometer with a graphite monochromatized Cu$K\alpha$ radiation. Diffraction data were collected at room temperature by step scanning over an angular range of $21° \leq 2\theta \leq 122°$ in increments of 0.02° (2θ), and with a counting time of 1 sec for each step. The simulation of the X-ray powder diffraction pattern and the Rietveld analysis were made with the program DBW 3.2S, which is an improved version of DBW 3.2 (17). The pseudo-Voigt peak-shape function without preferred crystallite orientation was used. The refined parameters were the scale factor, background parameters, 2θ zero-point, lattice constants, profile half-width parameters (U, V, W), the mixing parameters of the pseudo-Voigt function (NA, NB), asymmetry correction factor (P), occupancy, atomic fractional positions, and isotropic thermal parameters.

The magnetic susceptibility was measured with a Faraday-type magnetobalance in the temperature range from 77 to 300 K. The electron paramagnetic resonance spectra were obtained at 77 and 295 K by a Bruker ESR-300S microwave bridge X-band spectrometer.

X-ray absorption experiments for the Ta L_{III} edge were carried out on Beam Line 10B of the Photon Factory at the National Laboratory for High Energy Physics (KEK-PF, Tsukuba) using a Si(311) channel cut monochromator which gives an energy resolution of about 1 eV at 10 keV. The electron energy of the storage ring was 2.5 GeV at a current of between 250 and 350 mA. The K absorption edge of a copper foil at 8980.3 eV was used to calibrate the energy scale. All measurements were made in the transmission mode at room temperature. Sample thickness for absorption measurements was adjusted to give an edge step $\Delta\mu x \cong 1.5$ without considering the height of the white line for L_{III} edge absorption, and the step size over the edge was 0.5 eV.

RESULTS AND DISCUSSION

(*I*) *Structural Analysis*

X-ray powder diffraction data collected for Ca_2CrTaO_6 at room temperature seemed to be in agreement with the body-centered orthorhombic structure previously reported (1, 18, 19) for ordered $Ca_2BB'O_6$-type perovskites, but some peaks with very low intensity (indicated by arrows in Fig. 1) could not be successfully indexed with the body-centered structure. In this study, we found that Ca_2CrTaO_6 has a monoclinically distorted perovskite structure, with space group $P2_1/n$ (No. 14) having unit cell parameters of ca. $\sqrt{2}\ a_p \times \sqrt{2}\ a_p \times 2\ a_p$ and $\beta \approx 90.0°$, where a_p is the unit cell parameter of a simple cubic perovskite. This space group permits ordering of the Cr(III) and Ta(V) cations over the 6-coordinate sites of the perovskite structure. It should be noted that the lattice parameters can be considered those of a pseudo-orthorhombic lattice, and the B-site cation retains the body-centered orthorhombicity in this space group; however, only the calcium and oxygen ions lost the orthorhombic symmetry, so that the lattice symmetry was reduced to a monoclinic one. The ideal atomic coordinates [Ca 4(e) site was set to (0 0 $\frac{3}{4}$), O1 4(e) site to ($\frac{1}{4}$ $\frac{1}{4}$ 0), O2 4(e) site to ($\frac{1}{4}$ $\frac{1}{4}$ $\frac{1}{2}$), and O3 4(e) site to (0 $\frac{1}{2}$ $\frac{3}{4}$)] were used as starting values in the Rietveld refinements. After successive refinements of the profile parameters (U, V, W, NA, NB, P), the occupancy of Cr and Ta ions, the positional parameters for calcium and then for oxygens, and the isotropic thermal factors for all metal ions, the R values were lowered to $R_p = 5.60\%$, $R_{wp} = 8.46\%$. The temperature factors for each ion were refined with a constraint on the equality of the thermal parameters of Cr and Ta ions in the same position, while those for all oxygen ions were fixed to a value of 0.1. The occupancies of Cr and Ta ions were refined with a constraint that the overall atomic stoichiometry of Cr and Ta ions is 1 : 1. Neither refining the thermal parameters of oxygen ions nor releasing the constraint on the Cr and Ta occupancies led to any sig-

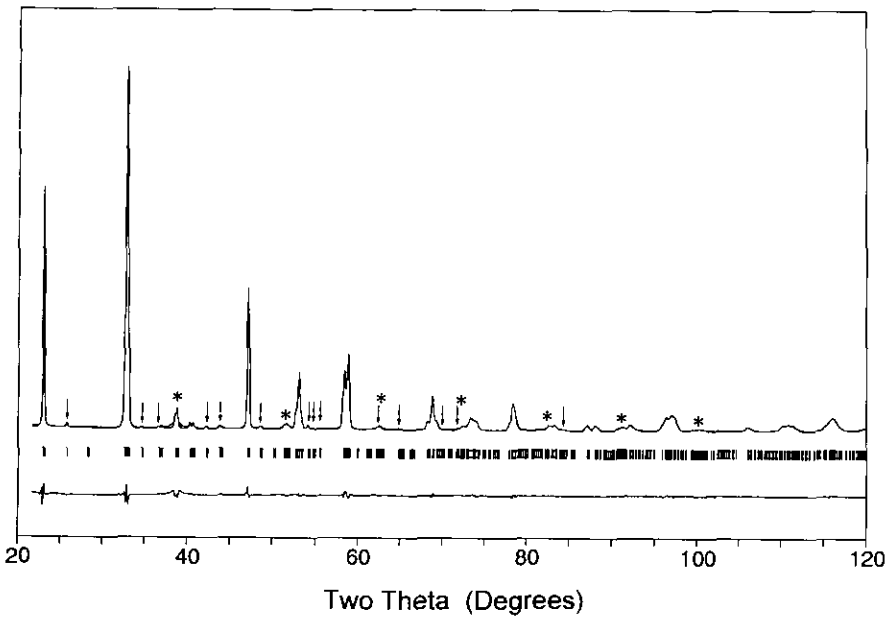

FIG. 1. Observed (···), calculated (—), and difference profiles for Ca_2CrTaO_6. The lines denoted by asterisks are superlattice lines showing the ordering of Cr and Ta ions. Those indicated by arrows confirm the monoclinic space group, which could not be indexed by any body-centered orthorhombic structure.

TABLE 1
Structure and Profile Parameters for Ca_2CrTaO_6 at Room Temperature (Standard Deviation in Parentheses)

Atom	Site	x	y	z	Occupancy	B(Å^2)
Ca	4*e*	0.007(2)	0.0390(4)	0.7504(8)	1	1.11(4)
Cr(1)	2*c*	0	½	0	0.726(3)	0.28(4)
Cr(2)	2*d*	½	0	0	0.274(3)	0.00(2)
Ta(1)	2*c*	0	½	0	0.274(3)	0.28(4)
Ta(2)	2*d*	½	0	0	0.726(3)	0.00(2)
O1	4*e*	0.278(2)	0.301(3)	0.958(3)	1	0.1
O2	4*e*	0.299(3)	0.279	0.540(3)	1	0.1
O3	4*e*	0.919(2)	0.477(1)	0.739(2)	1	0.1

Cell parameters: a = 5.4199(1)Å, b = 5.4936(1)Å, c = 7.7108(2)Å, β = 90.02(1)°
Space group: $P2_1/n$ (no. 14)
2θ range: 22–122°
Number of reflections: 778
Number of parameters: 34 (16 structural parameters)
Profile parameters (definition in (17)):
U = 0.220(10) V = −0.086(7) W = 0.038(1)
NA = 0.294(12) NB = 0.002(2) P = 0.096(2)
R-factors: R_p = 5.60%; R_{wp} = 8.46%; R_{exp} = 3.79%

$R_p = 100 \times \Sigma|Y_{obs} - Y_{calc}|/\Sigma Y_{obs}$; $R_{wp} = 100 \times \Sigma w|Y_{obs} - Y_{calc}|^2/\Sigma w|Y_{obs}|^2$; $R_{exp} = 100 \times (N - P + C)/\Sigma w|Y_{obs}|^2$; Y_{obs}, observed intensity, Y_{cal}, calculated intensity and $n - p + c$ = number of observations − number of variables + number of constraints.

nificant improvement in the R factors. The final atomic coordinates, occupancies, and thermal parameters are reported along with the profile parameters in Table 1. The most important bond distances and angles are calculated in Table 2. The observed, calculated, and difference profiles are shown in Fig. 1.

All the peaks in the diffraction pattern for Sr_2CrTaO_6

TABLE 2
Interatomic Distances (Å) and Bond Angles (°) for Ca_2CrTaO_6 (B = Cr-Rich (2*c*) Site, B' = Ta-Rich (2*d*) Site)

	Distances		
B–O1	1.890(26) × 2	B'–O1	2.070(23) × 2
B–O2	1.906(26) × 2	B'–O2	2.048(26) × 2
B–O3	2.064(27) × 2	B'–O3	1.899(18) × 2
Average B–O	1.953	Average B'–O	2.006
B–B'	3.859 ((001) plane)		
	3.855 (c-axis)		
Average B–B'	3.857		
Shortest O–O contact: O1–O2 2.66(4)			

Ca–O1	Ca–O2	Ca–O3
3.306(41)	3.288(44)	3.131(23)
2.719(40)	2.2694(43)	3.125(12)
2.606(41)	2.399(43)	2.455(13)
2.377(41)	2.377(41)	2.335(23)

Average Ca–O 2.734

		Angles			
B–O1–B'	154	O1–B–O2	89, 91	O1–B'–O2	89, 91
B–O2–B'	154	O1–B–O3	88, 92	O1–B'–O3	88, 92
B–O3–B'	153	O2–B–O3	89, 91	O2–B'–O3	90, 90

TABLE 3
Structural and Profile Parameters for Sr_2CrTaO_6 at Room Temperature (Standard Deviation in Parentheses)

Atom	Site	x	y	z	Occupancy	B(Å^2)
Sr	8c	$\frac{1}{4}$	$\frac{1}{4}$	$\frac{1}{4}$	1	0.84(3)
Cr(1)	4a	0	0	0	0.664(4)	−0.01(5)
Cr(2)	4b	$\frac{1}{2}$	$\frac{1}{2}$	$\frac{1}{2}$	0.336(4)	0.0(1)
Ta(1)	4a	0	0	0	0.336(4)	−0.01(5)
Ta(2)	4b	$\frac{1}{2}$	$\frac{1}{2}$	$\frac{1}{2}$	0.664(4)	0.0(1)
O	24e	0.2495(11)	0	0	1	0.5(1)

Cell parameter: a = 7.8837(1) Å
Space group: $Fm\bar{3}m$ (no. 225)
2θ range: 21–121°
Number of reflections: 66
Number of parameters: 21 (6 structural parameters)
Profile parameters: (definition in (17))
U = 0.0567(33) V = −0.032(4) W = 0.0280(10))
N_A = 0.186(130) N_B = 0.00614(27) P = −0.148(22)
R-factors: R_p = 8.52%; R_{wp} = 11.84%; R_{exp} = 3.65%

Note. R-factors are defined in Table 1.

TABLE 4
Interatomic Distances (Å) and Bond Angles (°) for Sr_2CrTaO_6 (B = Cr-Rich (4a) Site, B' = Ta-Rich (4b) Site)

Distances	
B–O	1.967(9)
B'–O	1.975(9)
Sr–O	2.787
B–B'	3.942
Shortest O–O contact:	2.782(12)
Angles	
B–O–B'	180
B–O–Ca	90.1(2)
B'–O–Ca	89.9(2)

at room temperature could be indexed by an ordered perovskite structure in the cubic space group $Fm\bar{3}m$ (No. 225) with a doubled unit cell parameter of a simple perovskite lattice. The ideal atomic coordinates of a cubic ordered perovskite were used as starting values in the Rietveld method. As in the case of Ca_2CrTaO_6, the occupancies of Cr and Ta ions were also refined. Isotropic thermal factors (B) were refined for all the atoms. The Rietveld refinement converged to give the conventional R factors R_p = 8.52% and R_{wp} = 11.84%. The final atomic coordinates, occupancies, and thermal parameters are presented in Table 3 along with the profile parameters. The observed, calculated, and difference profiles are shown in Fig. 2, and the bond distances and angles are calculated in Table 4.

(*II*) *Size Effect*

Most perovskites of the type $Ca_2B^{III}TaO_6$ (13, 18, 19) are known to have distorted structures, while those of the type $Sr_2B^{III}TaO_6$ (1, 14, 15, 20–23) have cubic or slightly distorted structures. Table 5 shows the Shannon ionic radii (24), the lattice constants, and the perovskite parameter $\bar{a}$, defined as the cube root of the cell volume of perovskite unit ABO_3, for $A_2B^{III}TaO_6$ (A = Ca and Sr). Such a distinct difference in structure between Ca and Sr compounds seems to arise from the difference in the ionic

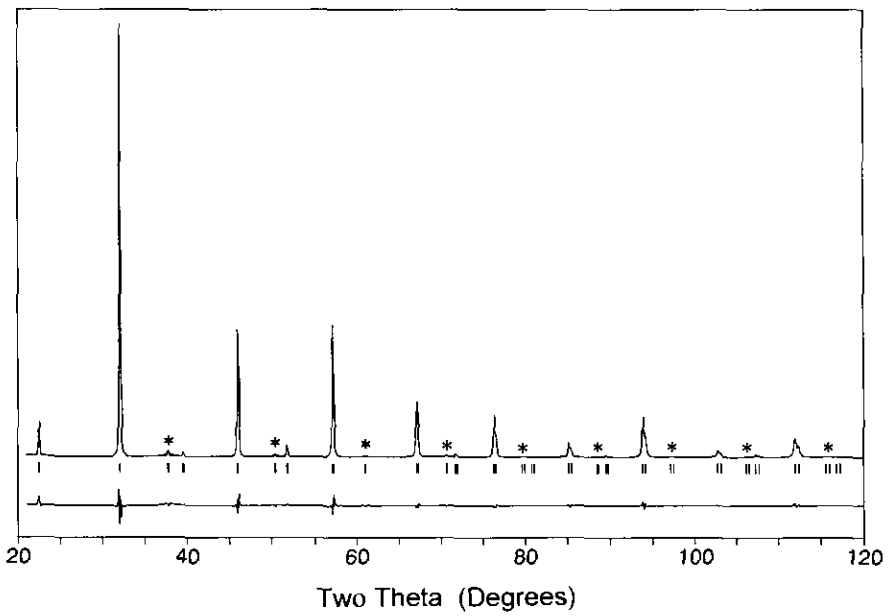

FIG. 2. Observed (···), calculated (—), and difference profiles for Sr_2CrTaO_6. The lines denoted by asterisks are superlattice lines showing the ordering of Cr and Ta ions.

TABLE 5
Lattice Constants and Perovskite Parameters ($\bar{a} = 3\sqrt{V_p}$) of A_2B(III)TaO_6, Where A = Ca and Sr

		A = Ca				A = Sr				
B	r(B) (Å)	a (Å)	b (Å)	c (Å)	$\bar{a}$ (Å)	a (Å)	b (Å)	c (Å)	β (°)	$\bar{a}$ (Å)
Al	0.535	5.381	5.407	7.612	3.811	7.786				3.893
V	0.64	5.45	5.49	7.76	3.872	3.967				3.967
Cr	0.615	5.4199 β = 90.02°	5.4936	7.7108	3.858	7.8825				3.941
Mn	0.645	5.462	5.571	3.873	3.891	3.994				3.994
Fe	0.645	5.451	5.56	3.88	3.889	3.981				3.981
Ga	0.62	5.543	5.493	7.704	3.885	7.892				3.946
In	0.80	5.537	5.697	7.938	3.971	8.11				4.055
Rh	0.665					7.936				3.968
Y	0.90	5.578	5.814	8.05	4.026					
Pr	0.99	5.632	5.87	8.124	4.065	5.87	5.98	8.35	90.15	4.185
Nd	0.983	5.62	5.864	8.113	4.058	5.86	5.96	8.34	90.15	4.176
Sm	0.958	5.592	5.861	8.092	4.047	5.85	5.93	8.31	90.18	4.161
Eu	0.947	5.581	5.855	8.086	4.042	5.84	5.91	8.30	90.20	4.153
Gd	0.938	5.575	5.842	8.063	4.034	5.83	5.90	8.29	90.22	4.146
Tb	0.923	5.574	5.832	8.057	4.031	5.82	5.88	8.28	90.15	4.138
Dy	0.912	5.576	5.82	8.052	4.027	5.82	5.87	8.26	90.13	4.132
Ho	0.901	5.577	5.806	8.045	4.023	5.81	5.85	8.23	90.13	4.120
Er	0.89	5.574	5.796	8.032	4.018	5.80	5.84	8.23	90.07	4.115
Tm	0.88					8.200				4.100
Yb	0.868	5.574	5.759	8.007	4.005	8.196				4.098
Lu	0.861	5.565	5.753	7.997	4.000	8.18				4.090

size of Ca and Sr ions. The perovskite structure may be described as a cubic close packing of oxygen ions, one-quarter of which have been replaced by larger cations (e.g., Ca or Sr in this case), and the octahedral site surrounded by oxygen ions is occupied by smaller cations. From this point of view, the distortion in Ca compounds appears to result from the small ionic size of the Ca ion relative to that of the oxygen ion. It was also supposed that in distorted perovskite structures the shifts and arrangements of large cations such as the A-site ion play a major role in such lattice deformations, and oxygen ions will only adjust and compensate for the shifts of A ions in lattice and electric charge (25). The tolerance factors for Ca_2CrTaO_6 and Sr_2CrTaO_6 are 0.9556 and 0.9905, respectively. As can be expected, the small ionic size of the Ca ion induces a smaller tolerance factor, which seems to be responsible for the distortion of Ca_2BTaO_6-type compounds. The distortion in some Sr_2BTaO_6-type compounds seems to arise from the relatively large B cations, which also produce small tolerance factors. In Fig. 3, the perovskite parameter, $\bar{a}$, is plotted against the ionic radius of the B(III) ion for both perovskites. For a given A cation (Ca or Sr), the perovskite parameters follow the linear relationship $\bar{a} = f(r_B)$, implying that the lattice constants are slightly in proportion to the metal ionic size. Therefore, it could be confirmed that the crystal structure of perovskite is chiefly dependent upon the size of the A-site cation, and the cell volume is more or less changed by the size of the B-site cation.

(III) *Partial Disordering of B/B' Cations*

It should be noted that the Cr and Ta ions in Ca_2CrTaO_6 and Sr_2CrTaO_6 are partially disordered at the 6-coordinated sites. In both cases, the superlattice lines (indicated

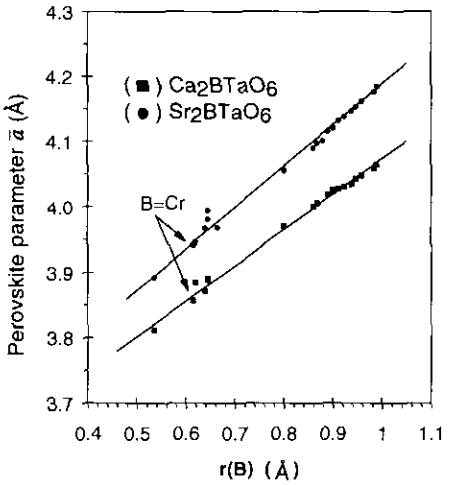

FIG. 3. The linear relationship between the cube root of the cell volume of the perovskite unit and the ionic radii of B(III) cations for Ca_2BTaO_6 and Sr_2BTaO_6 perovskites.

by asterisks in Figs. 1 and 2) due to the rock-salt arrangement of Cr and Ta ions at the 6-coordinate site were observed in X-ray diffraction patterns, but the peaks were found to be quite broad and diffuse compared to the other lines; furthermore, the observed intensities were much weaker than the calculated intensities based on the complete ordering of such ions. At first, it was thought that the reaction did not arrive at equilibrium. However, further reaction at high temperature did not make any difference in the broadness and weakness of the superlattice lines. This implies that the ordering of Cr and Ta ions is not complete. Thus, the partial disordering was assumed to be reasonable, and the degree of disordering was calculated by refining the occupancies of the ions with the constraint that the overall atomic ratio of Cr and Ta ions is 1 : 1. The refined results indicated that 2(*c*) and 4(*a*) sites are Cr-rich sites, where ca. 27 and 36% of Cr ions are replaced by Ta ions in Ca and Sr compounds, respectively (see Tables 2 and 4 for Ca and Sr, respectively). It is well known that an ordered arrangement between the *B* and the *B'* ions is common for the perovskite-type $A_2BB'O_6$ oxides when the difference in charge and ionic radii between them is large (26). Sr_2FeTaO_6 (14, 15), and Sr_2MnTaO_6 (20, 21), and Sr_2VTaO_6 (23) are well-known examples of the disordered perovskite, while Sr_2BTaO_6 (*B* = Al, Ga, In, Rh, Pr, Nd, Sm, Eu, Gd, Tb, Dy, Ho, Er, Tm, Yb, Lu) (1, 22) are ordered perovskites. It is generally believed that the Madelung energy is the main driving force for *B*-site cation ordering in the $A_2BB'P_6$-type perovskite. According to Rosenstein (27), the energy due to charge ordering can be a significant fraction of the total Madelung energy; in the case of $Ba_2Li^{I}Re^{VII}O_6$, the fraction is greater than 13%. However, in the case of $Ba_2Sc^{III}Re^{V}O_6$, the fraction is less than 2%. Thus, the Madelung energy gain would not contribute greatly to cation ordering in the $A_2B^{III}B^{V}O_6$-type perovskite. Furthermore, a contribution from entropy ($T\Delta S$) would favor the disordered structure. Therefore, the partial disordering of Cr and Ta ions in A_2CrTaO_6 (*A* = Ca, Sr) can be explained by two contributing factors such as small Madelung ordering energy and the tendency toward increasing entropy.

(IV) Covalency Effect

The octahedral environment of Cr and Ta ions is represented in Figs. 4a and 4b for Ca_2CrTaO_6 and Sr_2CrTaO_6, respectively. It is worth noting here that, although the unit cell is distorted significantly in the Ca compound (Fig. 4a), the octahedral environment surrounding the Cr and Ta ions is still preserved. Furthermore, it is surprising that the *B*–O distances are shorter than the *B'*–O distances since we expected that the oxygen ion might shift largely

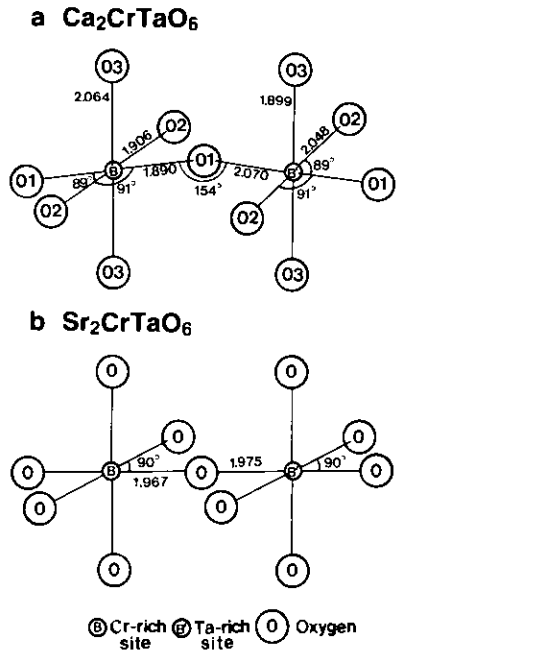

FIG. 4. The *B*-site cation environment of Ca_2CrTaO_6 (a) and Sr_2CrTaO_6 (b).

toward the Ta(V) ion due to its high charge. The same result was obtained for the Sr compound, although the difference between the two distances is reduced (Fig. 4b). In the ordered-type perovskite $A_2BB'O_6$, a shift of oxygen ions from their ideal position might arise from two main factors: (i) electrostatic energy (or ionic character) and (ii) electronic energy (or covalency between the *B* (or *B'*)–O bond). The consideration of electrostatic energy alone will always allow us to expect the shift of oxygen ions toward more highly charged Ta(V) ions, but the consideration of covalency will not always allow us to do so. Cr(III) and Ta(V) cations with outer electronic configurations d^3 and d^0 in an octahedral field can hybridize empty (d^2sp^3) orbitals for coordinate covalency with neighboring oxygen $2p_\sigma$ orbitals to form σ(*B*–O) bonds, and the half-filled (d^3) and empty (d^0) t_{2g} orbitals participate in π(*B*/*B'*–O) bonds with neighboring oxygen $2p_\pi$ orbitals. The oxygen $2p_\sigma$ and $2p_\pi$ orbitals represent atomic 2*p* orbitals in symmetry-adapted ligand group orbitals with e_g and t_{2g} symmetry, respectively. On the other hand, the covalent component of the *A*–O bond competes directly with the π(*B*/*B'*–O) bond. In this case the smaller Ca ion has the greater covalency component in the Ca–O bond, which would make the π component of the covalent *B*/*B'*–O bond smaller in the Ca compound than in the Sr compound.

Figure 4a shows that the *B'*–O–*B* angle in Ca_2CrTaO_6 is 154°. Since an oxygen 2*p* orbital forms a σ-bond not only with the *B* cation but also with the *B'* cation, such

a tilting geometry will make it difficult to form a linear σ-bond between the $2p$ orbital of intermediate O and the hybrid d^2sp^3 orbitals of B/B' cations; that is, such a bending geometry is inadequate to produce simultaneous covalent bondings on opposite sides of the O. Thus, one strong covalent bond in the $\sigma(B\text{–O})$ or $\sigma(B'\text{–O})$ bond will inhibit the formation of the other. From this point of view, the σ(Cr–O) covalency is stronger than the σ(Ta–O) one, as seen from the fact that the oxygen ions are shifted to a Cr-rich site, overcoming the stronger electrostatic force at the highly charged Ta-rich site. On the other hand, the cubic symmetry of BO_6 or $B'O_6$ octahedra and the linear $B'\text{–O–}B$ bond in Sr_2CrTaO_6 will make it much easier for the O $2p$ orbitals to form a σ-bond simultaneously with two B-site cations on opposite sides. Then two linear B–O and B'–O bonds will compete with each other in opposite directions so that the oxygen ion is approximately in the equilibrium position between the two B-site cations. Consequently, it is concluded that in spite of its lower valence the Cr(III) ion in the octahedral environment forms a much stronger covalent bond with the neighboring oxygen ion than the Ta(V) ion, producing relatively short Cr–O bond distances.

(V) *XANES Spectroscopy*

XANES of the Ta L_{III} edge was measured in order to obtain direct information on the evolution of covalency in the Ta–O bond because XANES spectroscopy is very useful for probing the electronic density of final states of the photoexcited core electrons (30). The spectra for the Cr L_{III} edge were not available since the energy of the Cr L_{III} edge is below the measurement range of the beam line we used. The appearance of a strong peak just above the X-ray absorption edge, which is referred to as the "white line" for historical reasons, has been an interesting subject (31). The origin of the white line is usually explained by electronic transition to the final state with a high density. The X-ray absorption coefficient (μ) in the electric dipolar approximation can be expressed as

$$\mu = \frac{4\pi^2\omega e^2}{c} N_a|\langle\psi_i|r|\psi_f\rangle|^2\rho(E_f)$$

by Fermi's golden rule (32), where c is the velocity of light, N_a is the number of absorbing atoms per unit volume, $\langle\psi_i|r|\psi_f\rangle$ is the radial dipole matrix element between initial and final states, and $\rho(E_f)$ is the density of the unoccupied final state. The dipole selection rules are $\Delta l = \pm 1$ and $\Delta j = 0, \pm 1$, and in the one-electron model the white line of the X-ray absorption L_{III} edge corresponds to the transition from $2p_{3/2}$ to $nd_{3/2,5/2}$. Since the outermost atomic states (usually d state) are considerably influenced by the degree of covalency between the transition metal and the oxygen ions, the degree of the covalency will be reflected on the white line intensity at the Ta L_{III} edge (33, 34). According to the above equation, the white line intensity is proportional to the radial dipole matrix element, and it was derived by Rao *et al.* (33), by the quantitative investigation on the Nd^{III} L_{III} edge using the Slater wave function along with necessary screening constants, that an increased covalency results in a larger matrix element. A comparison of the XANES at the Ta L_{III} edge for the present system is shown in Fig. 5. After a pre-edge background subtraction the edge jumps of the spectra are normalized to unity, averaging the signal to about 50 eV above the white line. The splitting into two peaks at the edge is characteristic at the L_{III} edge of all d^n compounds due to the transitions from $2p_{3/2}$ to t_{2g} and e_g orbitals (35, 36). The inflection points of the two edges, corresponding to the valence of the transition metal ion, are within about 0.5 eV of one another, which is within the limit of experimental error. As can be seen in Fig. 5, the white line intensity is almost the same with slightly lower intensity in the Sr compound, implying a slightly weaker Ta–O bond than that in the Ca compound if we neglect the sample thickness effect. Such an appearance can be explained if we suppose that the Cr–O covalency is intrinsically stronger than that of Ta–O as could be deduced in structural analysis; the high symmetry in the Sr compound will maximize the coordinate overlap between all Cr–O networks in the lattice through σ and increased π bondings, but the distortion in the Ca compound will produce a relatively weak Cr–O covalency at the Ta-rich site of the partially disordered lattice. Thus, the average Cr–O covalency in the Sr compound is thought to be stronger

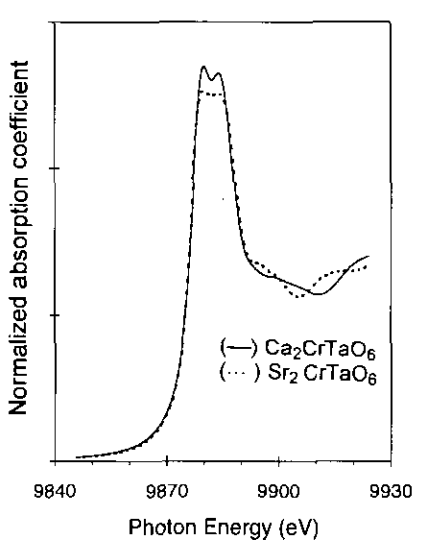

FIG. 5. Normalized Ta L_{III} edge for Ca_2CrTaO_6 (—) and Sr_2CrTaO_6 (···).

than that in the Ca compound, which will induce a relatively weak average Ta–O covalency in the Sr compound.

(VI) Magnetic Study

The electron paramagnetic resonance (EPR) spectra were obtained at 295 and 77 K. All the observed signals were isotropic, and the observed g and ΔH values are presented in Fig. 6 and are also compared with those of other Cr-containing oxides in Table 6 (37–41). The g values of A_2CrTaO_6 (A = Ca and Sr) at 300 K are slightly lower than those of other compounds. Such small negative deviations of the g value may result from the enhanced interaction of Cr(III) ions at the B-site with a disordered arrangement of Cr(III) and Ta(V) ions in the lattice, although the strength of interaction seems to be very weak as can be seen from the sharp isotropic EPR signals.

It should be noted that at room temperature the Ca compound has a larger ΔH value than the Sr compound. The dipole–dipole interaction between magnetic ions (Cr) and the distortion of local symmetry inducing the change of the local magnetic field can be the sources of the line broadening, but such a magnetic interaction seems to be negligible in both compounds at room temperature. Thus, the larger ΔH in the Ca compound might result from the distortion of local symmetry of CrO_6 in Ca_2CrTaO_6. The EPR signal for the Ca compound becomes sharper at a lower temperature (77 K), as expected; in contrast, the signal for the Sr compound is broadened. Such a broadening could be attributed to the possible magnetic interaction

TABLE 6
The g Values of Cr(III) Stabilized in Various Oxygen Lattices at Room Temperature

Compound	g	Ref.
Ca_2CrTaO_6	1.965(2)	This work
Sr_2CrTaO_6	1.970(1)	This work
Cr(III)/ZrO_2	1.98	(37)
Cr(III)/Cs_2NaAlF_6	1.975	(38)
Cr(III)/MgO	1.9782(3)	(39)
Cr(III)/$Cd_2Nb_2O_7$	1.9723	(40)
Cr(III)/$SrTiO_3$	1.9788(7)	(41)

between nearest-neighbor Cr ions at lower temperature through $Cr(t_{2g})$–$O(p_\pi)$–$Cr(t_{2g})$ in the partially disordered lattice. Such interaction will be enhanced if the π $(t_{2g}$–$p_\pi)$ bond strength increases. Because the Sr compound has highly symmetric BO_6 and $B'O_6$ octahedra and oxygen ions are approximately in equilibrium position between two B-sites, a maximum overlap between t_{2g} and p_π orbitals will be produced, whereas the bending of the B–O–B' bond from 180° reduces the strength of the Cr–O–Cr interactions in the Ca compound. Moreover, the Sr ion being less covalent than the Ca ion would enhance the competing $\pi(t_{2g}$–$p_\pi)$ bond in a cubic Sr compound. Consequently, the broadening EPR signal at low temperature for the Sr compound can be ascribed to increased magnetic interaction through strong $\pi(t_{2g}$–p_π–$t_{2g})$ covalent bonding at lower temperature.

In Fig. 7, the temperature dependence of inverse molar magnetic susceptibilities is shown. The diamagnetic contribution of every ion is corrected according to Selwood (42). Both perovskites follow the Curie–Weiss law between 77 and 300 K, with Curie constants of C = 1.60

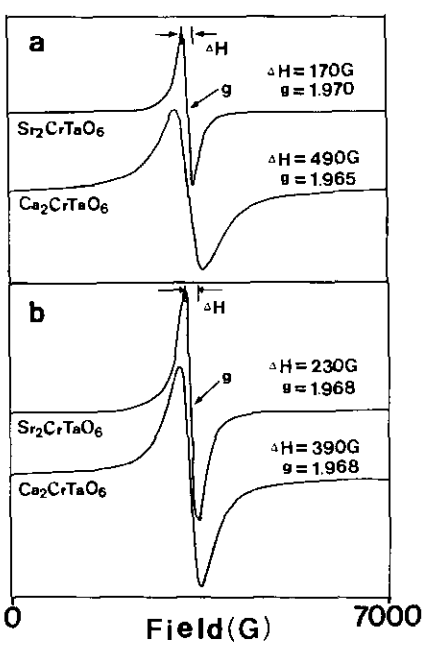

FIG. 6. The EPR spectra of Ca_2CrTaO_6 and Sr_2CrTaO_6 at 295 K (a) and 77 K (b).

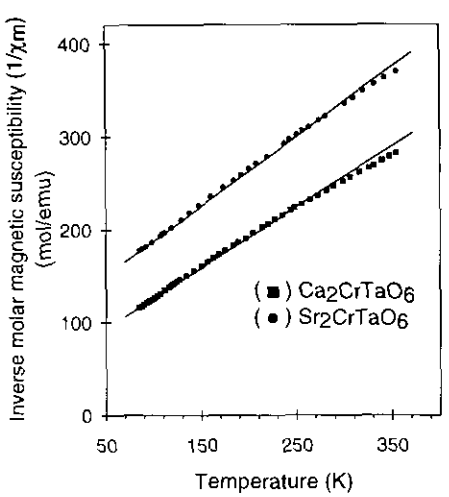

FIG. 7. The temperature dependence of inverse molar magnetic susceptibilities of Ca_2CrTaO_6 and Sr_2CrTaO_6.

and 1.37, Weiss constants of $\theta = -104$ and -161 K, and effective magnetic moments (μ_{eff}) of 3.76 μ_B and 3.67 μ_B for the Ca and Sr compounds, respectively. The C and θ were obtained from the least-squares fit of $\chi_m^{-1} = (T - \theta)/C$. The observed magnetic moments are consistent with the spin-only value for Cr(III) (3.87μ_B), and the smaller magnetic moment for the Sr compound seems to be due to the enhanced $\pi(t_{2g}-p_\pi-t_{2g})$ interactions.

CONCLUSION

According to the present X-ray analysis, we have found that the crystal symmetry for Ca_2CrTaO_6 reported in the literature (orthorhombic) was wrong. The perovskites Ca_2CrTaO_6 and Sr_2CrTaO_6 have been found to have space groups of $P2_1/n$ (monoclinic, a = 5.4199(1) Å, b = 5.4936(1) Å, c = 7.7108(2) Å, and β = 90.02(1)°) and $Fm\bar{3}m$ (cubic, a = 7.8837(1) Å), respectively. The Cr and Ta ions are partially disordered in these perovskites, which might be attributed to the small Madelung ordering energy and the tendency toward increasing entropy. Rietveld analysis indicated that the Cr–O bond distance is more or less shorter than the Ta–O distance in both compounds. Such a result can be explained by two factors, the size of the A cation and the strong covalency of the Cr–O bond. In the case of Ca_2CrTaO_6, the small size of the Ca ion induces a strong lattice distortion which prohibits a linear $\sigma(B$–O) and $\sigma(B'$–O) bond formation. On the other hand, in the case of the Sr compound, the size of the Sr ion is quite adequate and that of the Cr and Ta ions is small enough for a cubic perovskite structure, which enables the maximum overlap of the σ and π bonds in the lattice. In addition, the less covalent Sr–O bond induces a stronger π bond. Given that Cr–O bond distances are shorter than Ta–O ones in spite of the lower valence of Cr(III) than of Ta(V), it could be proposed that Cr–O covalency is relatively stronger than Ta–O covalency. The variation of EPR line broadening and magnetic moments with temperature could also be explained by the variation of the π(Cr–O) bond in the two compounds.

ACKNOWLEDGMENTS

This work is supported by the S.N.U. Daewoo Research Fund (93-05-2072) and the Korea Science and Engineering Foundation (92-25-00-02). We thank the PLS (Korea) for the funding of the synchrotron radiation experiment at Tsukuba. We also thank Professor M. Nomura at the Photon Factory for his assistance with the XANES measurement.

REFERENCES

1. J. B. Goodenough, W. Gräper, F. Holtzberg, D. L. Huber, R. A. Lefever, J. M. Longo, T. R. McGuire, and S. Methfessel, Eds., "Magnetic and Other Properties of Oxides and Related Compounds," Landolt–Boernstein Numerical Data & Functional Relationships in Science & Technology (K. H. Hellwege and A. M. Hellwege, Eds.), New Series, Group 3: Crystal & Solid State Physics, Vol. 4, Part A. Springer-Verlag, Berlin/Heidelberg/New York, 1970.
2. J. H. Choy and S. T. Hong, *Bull. Korean Chem. Soc.* **10,** 8 (1989).
3. J. H. Choy and S. T. Hong, *J. Chem. Soc., Dalton Trans.*, 2335 (1989).
4. G. Blasse, *J. Inorg. Nucl. Chem.* **27,** 993 (1965).
5. H. Thomann, *Ferroelectrics* **73,** 183 (1987).
6. M. T. Barriuso, J. A. Aramburu, M. Moreno, M. Flórez, G. Fernández Rodrigo, and L. Pueyo, *Phys. Rev. B* **38,** 4239 (1988).
7. J. B. Goodenough, *Phys. Rev.* **164**(2), 785 (1967).
8. K. Allan, A. Campion, J. Zhou, and J. B. Goodenough, *Phys. Rev. B* **41,** 11572 (1990).
9. M. Takano, S. Nasu, T. Abe, K. Yamamoto, S. Endo, Y. Takeda, and J. B. Goodenough, *Phys. Rev. Lett.* **67,** 3267 (1991).
10. R. Claessen, M. G. Smith, J. B. Goodenough, and J. W. Allen, *Phys. Rev. B* **47,** 1788 (1993).
11. J. H. Choy, S. T. Hong, and S. G. Kang, *in* "Proceedings, International Symposium on Fine Ceramics, ARITA '89," p. 69, 1989; J. H. Choy, *New Ceramics* **4,** 87 (1991).
12. S. T. Hong, Ph.D. thesis, Seoul National University, 1994.
13. V. S. Filip'ev and E. G. Fesenko, *Sov. Phys.—Crystallogr.* (*Eng. Transl.*) **10,** 243 (1966).
14. S. Nomura and T. Nakagawa, *J. Phys. Soc. Jpn.* **30**(2), 491 (1971).
15. G. Patrat, M. Brunel, and F. de Bergevin, *J. Phys. Chem. Solids* **37,** 285 (1976).
16. Y. Torii, S. Kawamura, and R. Kurokawa, *Chem. Lett.* 1185 (1980).
17. D. B. Wiles and R. A. Young, *J. Appl. Crystallogr.* **14,** 149 (1981).
18. C. Chauvel, J. C. Bernier, and A. Michel, *C.R. Acad. Sci.* **262,** 1424 (1966).
19. H. Brusset, H. Gillier-Pandraud, and P. Rajaonera, *C.R. Acad. Sci.* **271,** C 810 (1970).
20. V. S. Filip'ev and E. G. Fesenko, *Sov. Phys.—Crystallogr.* (*Engl. Transl.*) **6,** 616 (1961).
21. M. F. Kupriyanov and V. S. Filip'ev, *Sov. Phys.—Crystallogr.* (*Engl. Transl.*) **8,** 278 (1963).
22. V. S. Fililp'ev and E. G. Fesenko, *Sov. Phys.—Crystallogr.* (*Engl. Transl.*) **10,** 532 (1966).
23. C. Chauvel, J. C. Bernier, and A. Michel, *C.R. Acad. Sci.* **263,** 1536 (1966).
24. R. D. Shannon, *Acta Crystallogr., Sect. A* **32,** 751 (1976).
25. T.Nakamura, *Mater. Res. Bull.* **13,** 1023–1030 (1978).
26. F. Galasso and W. Darby, *J. Phys. Chem.* **66,** 131 (1962).
27. R. D. Rosenstein and R. Schor, *J. Chem. Phys.* **38,** 1789 (1963).
28. J. B. Goodenough and A. L. Loeb, *Phys. Rev.* **98**(2), 391 (1955).
29. S. Sugano and R. G. Shulman, *Phys. Rev.* **130**(2), 517 (1963).
30. J. M. Tranquada, S. M. Heald, and A. R. Moodenbaugh, *Phys. Rev. B* **36,** 5253 (1987).
31. M. Brown, R. E. Peierls, and E. A. Stern, *Phys. Rev. B* **15,** 738 (1977).
32. D. C. Koningsberger and R. Prins, "X-Ray Absorption," Chap. 1. Wiley, New York, 1988.
33. K. J. Rao, J. Wong, and M. J. Weber, *J. Chem. Phys.* **78,** 6228 (1983).
34. G. G. Long, A. G. Revesz, and M. Kuriyama, *J. Non-Cryst. Solids* **70,** 271 (1985).
35. F. M. F. de Groot, J. C. Fuggle, B. T. Thole, and G. A. Sawatzky, *Phys. Rev. B* **41,** 928 (1990).
36. B. Poumellec, J. F. Marucco, and B. Touzelin, *Phys. Status Solidi B* **137,** 519 (1986).

37. A. Cimino, D. Cordischi, S. De Rossi, G. Ferrais, D. Gazzoli, V. Indovina, M. Occhiuzzi, and M. Valigi, *J. Catal.* **127,** 761 (1991).
38. E. Fargin, B. Leistienne, and J. M. Dance, *Solid State Commun.* **75**(10), 769 (1990).
39. B. Henderson and T. P. P. Hall, *Proc. Phys. Soc., London* **90,** 511 (1967).
40. S. Waplak and N. N. Kolpakova, *Phys. Status Solidi* **117,** 461 (1990).
41. L. Forni and C. Oliva, *J. Chem. Soc., Faraday Trans.* **84**(7), 2477 (1988).
42. P. W. Selwood "Magnetochemistry," 2nd ed., Chap. 5. Interscience, New York, 1967.